Generating Comparable and Fine-Scale Time Series of Summer Land Surface Temperature for Thermal Environment Monitoring

Yao Shen, Huanfeng Shen, *Senior Member, IEEE*, Qing Cheng, and Liangpei Zhang, *Fellow, IEEE*

***Abstract*—Satellite images have been widely used for urban heat island (UHI) monitoring in recent studies, among which the summer UHI has attracted more attention. However, the studies based on high spatial resolution images have to use single-day land surface temperature (LST) to analyze the summer UHI, due to the low temporal resolution, which is not representative of the summer and leads to incomparability in the time series. The studies based on low spatial resolution images can generate a time series of representative LSTs for summer (e.g., summer mean LSTs), due to the high temporal resolution, but these LSTs lack sufficient spatial details for a refined analysis. To fill these gaps, we propose to integrate the respective advantages of the above approaches to generate a comparable and fine-scale LST time series with a high spatiotemporal resolution. By normalizing the LSTs between the different satellite images via robust fitting with Huber's M-estimator and moment matching, the comparability is ensured. Furthermore, the high-spatial resolution and high-temporal resolution are combined via the spatiotemporal fusion. Overall, we propose a procedure to produce a comparable time series of annual and fine-scale summer mean LSTs, which can serve as a basis for elaborate analysis of the thermal environment.**

***Index Terms*—Land surface temperature (LST) normalization, remote sensing, spatiotemporal fusion, summer mean LST (SMLST).**

I. Introduction

UNDER the circumstance of global climate change [1]–[4], there is a need for us to establish the evolution of the thermal environment. If the history of the thermal environment can be interpreted, it may help us take action in the present day. Land surface temperature (LST), which is a result of surface-atmosphere interactions and energy budget considerations [5]–[7], is a key parameter for the monitoring of the thermal environment [8]. In particular, thermal phenomenon [e.g., urban heat island (UHI)] is likely to be more significant in summer [9], [10]. Thus, to thoroughly establish both the past and the present of the thermal environment, a long-term and fine-scale series of summer LST is required for an elaborate analysis [11], [12].

Given the wall-to-wall coverage of the land surface and the continuous operation [13], remotely sensed data have been widely used for long-term summer LST monitoring. Based on the spatial resolution of the satellite data used to monitor long-term LST, the current researches can be roughly classified into two categories. Some of the studies have taken high spatial resolution (high-resolution) images as the experimental data (e.g., Landsat). Such studies generally present their research results every few years. For example, every ten years, Qiao *et al.* investigated the spatiotemporal dynamics of summer LST in Beijing in China [14]; every eight years from 1984 to 2014, Yang *et al.* reported the summer LST changes in Changchun in China [15]; in 1985, 1992, 2001, 2008, and 2017, Weng *et al.* described the UHI pattern in Babol in Iran; and every two years from 1997 to 2008 [16], Li *et al.* monitor the patterns of the UHI in Shanghai in China [17]. The reason for such discontinuous monitoring lies in the low temporal resolution of the high-resolution images. As the high-resolution images have a relatively long revisit cycle, few observations can be obtained over the whole of the summer (except for the tropics). Furthermore, as a result of cloud or haze, it is likely that only one image or even no images may be available for the whole of the summer period. Hence, researchers have to select a single image to represent the whole of the summer for several years. However, the weather and soil conditions of the selected images are unlikely to remain the same for different years [18], so that the selected single-day LST cannot be recognized as representative LST for the summer, which leads to incomparability between the different summers.

The other category of studies takes coarse spatial resolution (coarse-resolution) images [e.g., moderate-resolution Imaging Spectroradiometer (MODIS)] as the experimental data. These studies can generate a summer mean LST (SMLST) for the whole of the summer for each year, due to the high temporal resolution [19]–[24]. For instance, Imhoff *et al.* [21] and Zhang *et al.* [20] described the summer UHI effect in American cities from 2003 to 2005; and Peng *et al.* generated summer UHI for 419 cities worldwide for a longer time series from 2003 to 2008. In this article, the continuous time series for LST in each summer serve as the basis for the mean LST of the whole

Manuscript received September 16, 2020; revised December 4, 2020; accepted December 19, 2020. Date of publication December 23, 2020; date of current version February 4, 2021. This work was supported in part by the National Key Research and Development Project of China under Grant 2019YFB2102900. *(Corresponding author: Huanfeng Shen.)*

Yao Shen is with the School of Resource and Environmental Sciences, Wuhan University, Wuhan 430072, China (e-mail: shenyao_sy@whu.edu.cn).

Huanfeng Shen is with the School of Resource and Environmental Sciences and the Collaborative Innovation Center for Geospatial Technology, Wuhan University, Wuhan 430072, China (e-mail: shenhf@whu.edu.cn).

Qing Cheng is with the School of Computer Science, China University of Geosciences, Wuhan 430074, China (e-mail: qingcheng@whu.edu.cn).

Liangpei Zhang is with the State Key Laboratory of Information Engineering in Surveying, Mapping and Remote Sensing, Wuhan University, Wuhan 430072, China (e-mail: zlp62@whu.edu.cn).

Digital Object Identifier 10.1109/JSTARS.2020.3046755

This work is licensed under a Creative Commons Attribution 4.0 License. For more information, see https://creativecommons.org/licenses/by/4.0/

of the summer [22]. The SMLST is representative enough so that the LST is comparable for different summers. However, the spatial resolution is too coarse to carry out more refined analysis (e.g., detailed distribution for the UHI effect). In summary, the inadequacy of the two categories lies in the trade-off between the spatial and temporal resolutions [25]–[28].

Therefore, it can be concluded that a single category of satellite images is not able to meet the demands of comparable and fine-scale time series for summer LST. An effective framework combining the comparability, high temporal resolution, and the high spatial resolution is thus required. To solve this problem, the spatiotemporal fusion technique is considered as a cost-effective way by blending observations from multiple sensors with different advantages or characteristics [29]–[31]. A number of studies have already focused on producing a high spatial and temporal LST time series by conducting spatiotemporal data fusion. For example, Shen *et al.* generated a long-term and fine-scale summer LST series for Wuhan in China by spatiotemporal fusion and image recovery, and were thus able to carry out a refined analysis of the UHI pattern evolution and LST changes with regard to land cover [25]; and Herrero–Huerta *et al.* generated a monthly and fine-scale LST series by spatiotemporal fusion so that a detailed UHI distribution could be established for each season [32]. However, in this articles, the summer LSTs were still represented by single-day or less than three-day LSTs, so that they could not be considered as a thorough description of summer LST.

To fill in these gaps, we have designed a procedure to produce time series of comparable and fine-scale SMLSTs. In particular, normalization is undertaken to reduce the difference and control the comparability between the different satellite images. The SMLST is skillfully calculated to ensure the representativeness of the summer LST and to control the comparability in the time series. Spatiotemporal fusion is also employed to combine the high temporal resolution and the high spatial resolution. Therefore, with the assistance of the high-resolution and coarse-resolution images, by integrating normalization and spatiotemporal fusion, a time series of comparable and fine-scale summer LSTs can be generated.

II. Study Region and Data

A. Study Region

Wuhan is located between 113°41′ E–115°05′ E and 29°58′ N–31°22′ N in China, with an administrative area of 8494.41 km^2, and a subtropical monsoon climate. As one of the hottest "stove cities" in China [33], [34], Wuhan can be considered as a typical city to study LST patterns in summer. Thus, Wuhan was selected as the experimental area in this article. The satellite data scene used in this research covers more than 80% of the Wuhan, including the whole of the Wuhan metropolis (see Fig. 1).

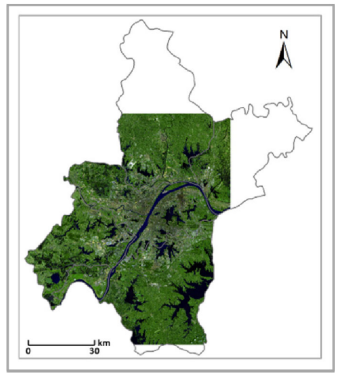


Fig. 1. Study area: Wuhan, in China. The image is the Landsat-8 image from September 15, 2018.

TABLE I
Data Used in This Research

Data	Dates
Landsat-5 (TM)	1987/09/26, 1988/08/11, 1989/03/07, 1990/09/02, 1991/07/19, 1992/04/16, 1993/10/12, 1994/05/08, 1995/08/31, 1996/10/04, 1997/09/21, 1998/10/26, 1999/09/27, 2000/09/13, 2002/09/03, 2003/05/01, 2004/07/22, 2005/04/20, 2006/11/01, 2008/04/20, 2009/09/06, 2010/11/12, 2011/06/08
Landsat-7 (ETM+)	2001/07/22
Landsat-8 (OLI/TIRS)	2013/06/13, 2014/10/06, 2015/10/25, 2016/07/23, 2017/10/30, 2018/09/15
MODIS	2000/09/13, 2001/07/22, 2002/09/03, 2003/05/01, 2004/07/22, 2005/04/20, 2006/11/01, 2009/09/06, 2010/11/12, 2011/06/08 MOD11A1 covering the whole summer in 2000-2018
AVHRR	1987/09/26, 1988/08/11, 1989/03/07, 1990/09/02, 1991/07/19, 1992/04/16, 1993/10/12, 1994/05/08, 1995/08/31, 1996/10/04, 1997/09/21, 1998/10/26, 1999/09/27 Surface reflectance covering the whole summer in 1984-2018
Water vapor (reanalysis data)	1987/09/26, 1988/08/11, 1989/03/07, 1990/09/02, 1991/07/19, 1992/04/16, 1993/10/12, 1994/05/08, 1995/08/31, 1996/10/04, 1997/09/21, 1998/10/26, 1999/09/27, 2000/09/13, 2001/07/22, 2002/09/03, 2003/05/01, 2004/07/22, 2005/04/20, 2006/11/01, 2008/04/20, 2009/09/06, 2010/11/12, 2011/06/08, 2013/06/13, 2014/10/06, 2015/10/25, 2016/07/23, 2017/10/30, 2018/09/15

B. Data

The data used included two main parts (see Table I).

1) *Satellite data*: Cloud-free Landsat images (Landsat 4/5/7/8) covering Wuhan were obtained for several months during 1984–2018 from the United States Geological Survey website.[1] The spatial resolution for the different Landsat thermal bands is 120 m [Landsat-4/5 thematic mapper (TM)], 60 m [Landsat-7 enhanced thematic mapper plus (ETM+)], and 100 m [Landsat-8 thermal infrared sensor (TIRS)], respectively, which were all resampled to a 30-m resolution when downloaded. From 2000 to 2018, the MOD11A1 product covering the whole of the summer (June 1, to August 31) and corresponding to the dates of the cloud-free Landsat images was obtained from the level-1 and atmosphere archive and distribution system distributed active archive center (LAADS DAAC) website.[2] The spatial resolution of the MOD11A1 product is 1000 m. The advanced very high resolution radiometer (AVHRR) surface reflectance product (version 4) covering the whole of the summer was collected from the National oceanic and atmospheric administration climate data record website.[3] The spatial resolution of the AVHRR surface reflectance product is 0.05°. From 1984 to 1999, the

[1][Online]. Available: http://glovis.usgs.gov/
[2][Online]. Available: https://ladsweb.modaps.eosdis.nasa.gov/
[3][Online]. Available:https://data.nodc.noaa.gov/

AVHRR surface reflectance product corresponding to the dates of the cloud-free Landsat images and covering the whole of the summer was also collected.

2) *Reanalysis data*: The water vapor data for LST inversion were obtained from the National Centers for Environmental Prediction (NCEP)/National Center for Atmospheric Research (NCAR) reanalysis dataset [35], with a spatial resolution of 2.5°.

The original Landsat data were calibrated into top-of-atmosphere radiance by the calibration coefficients provided by the satellite. Moreover, to alleviate the influence of atmospheric effects, the fast line-of-sight atmospheric analysis of spectral hypercubes atmospheric correction algorithm was applied to all the experimental images.

III. Methods

A. LST Retrieval

Since it is difficult to obtain real-time atmospheric profile data when the satellites pass through the study area over a long-term time series, especially before 2000, we chose a single-channel LST inversion method for the Landsat LST inversion for which only the radiance, emissivity and water vapor are needed [36]–[41]. The single-channel algorithm has been found to result in an accuracy within 1K in most cases [42], [43]. The normalized difference vegetation index (NDVI) was used to indicate the land cover so as to calculate the emissivity according to the method proposed by Sobrino *et al.* [44], [45]. The water vapor data were obtained from the NCEP/NCAR reanalysis dataset.

The AVHRR surface reflectance product contains the reflectance for the red band and near-infrared band (band 1 and band 2, respectively), and brightness temperature for the mid-infrared band (band 3) and thermal infrared bands (band 4 and band 5). A simple split-window LST algorithm was selected to retrieve AVHRR LST [46], [47], for which only the brightness temperature and the emissivity for the two thermal infrared bands of the AVHRR product are needed. Similar to the emissivity measured from Landsat, the emissivity for the AVHRR bands was also measured by the NDVI [45], [48]–[50].

B. Basic Idea of the Proposed Method

To carry out long-term and fine-scale monitoring of the thermal environment, high spatial and temporal resolutions for the LST time series are required. Thus, the spatiotemporal fusion method was used in this research to meet the requirement for a high spatiotemporal resolution. In brief, the spatiotemporal fusion method aims to add sufficient spatial details generated from the high-resolution images into the coarse-resolution images so that the high spatial resolution and high temporal resolution can be integrated. To conduct the spatiotemporal fusion, at least one pair of high-resolution and coarse-resolution images from the reference date (i.e., reference pair), and a coarse-resolution image from the target date (i.e., target image) are required (see Fig. 2). The high-resolution image from the reference date supplies effective spatial details, while the coarse-resolution images from the reference and target dates provide the spectral variation between the reference date and target date. In particular, the spatial and temporal nonlocal filter-based data fusion method

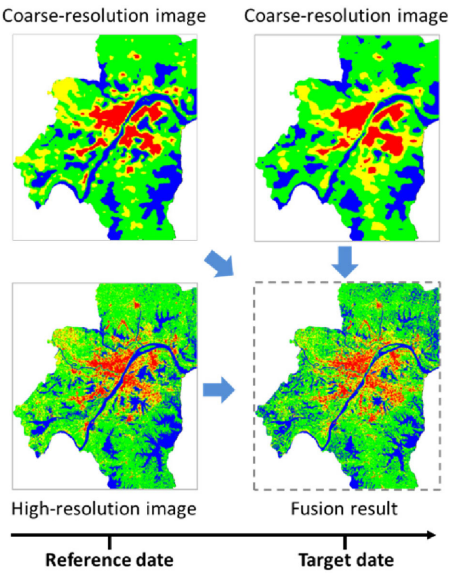


Fig. 2. Illustration of spatiotemporal fusion. For each image, the red area is the top 7.5% LST; the yellow area is the top 7.5%–25% LST; the green area is the top 25%–80% LST; the blue area is the last 20% LST.

(STNLFFM, software downlink)[4] was utilized to generate the LST time series with a high spatiotemporal resolution [31], [51]. Although STNLFFM was developed for use with reflectance data, its application for LST has been tested in previous research [25].

The STNLFFM predicts the high-resolution LST at the target date t_p with the assistance of the high-resolution and coarse-resolution LST at reference date t_k. The high-resolution LST can be retrieved from

$$F(x,y,t_p) = \sum_{i=1}^{N} W(x_i,y_i,t_k) \times [a(x_i,y_i,t_k) \times F(x_i,y_i,t_k) + b(x_i,y_i,t_k)] \quad (1)$$

where F denotes the high-resolution LST. (x, y) is a given pixel location. t_p is the target date. $F(x, y, t_p)$ is the predicted high-resolution LST of the target pixel (x, y) at t_p; N is the number of similar pixels (with the same land cover as the target pixel) within the image, including the target pixel itself. (x_i, y_i) is the location of the i th similar pixel. t_k is the reference date. $W(x_i, y_i, t_k)$ is the weight of the ith similar pixel at t_k. $F(x_i, y_i, t_k)$ is the LST in the high-resolution image for the ith similar pixel at t_k. $a(x_i, y_i, t_k)$ and $b(x_i, y_i, t_k)$ are the coefficients determined by the LST changes from date t_k to date t_p. The $W(x_i, y_i, t_k)$ describes the contribution of each similar pixel to the prediction of the high-resolution LST of the target pixel. For a detailed description of the calculation, we refer the reader to [31].

There are three inputs for the spatiotemporal fusion model, i.e., high-resolution (30 m) and coarse-resolution (1000 m) images at the reference date, and a coarse-resolution image at the target date. One high-resolution (30 m) output at target date. The most important step is to generate suitable inputs. The selection of the three inputs is discussed in the following sections. The

[4][Online]. Available: http://sendimage.whu.edu.cn

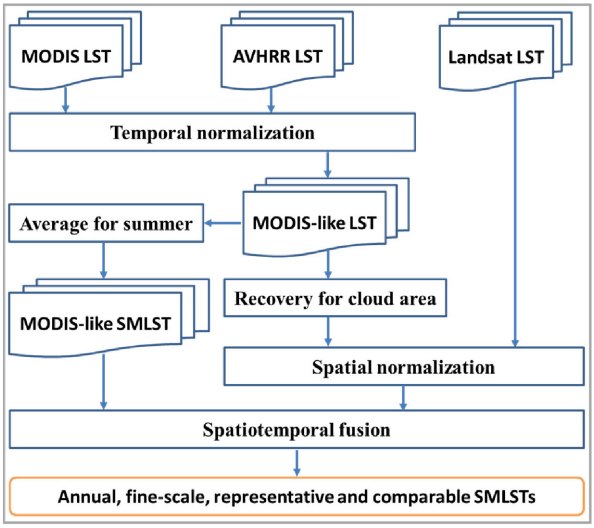


Fig. 3. Production procedure for comparable and fine-scale SMLSTs.

normalization methods used to assure the comparability are also discussed. The flowchart of the whole method is shown in Fig. 3.

C. Target Image Selection for Representativeness

To produce a more representative LST for the whole summer, we skillfully take the SMLST instead of single-day LST as the coarse-resolution image at the reference date. The SMLST is the average of all the LSTs in each summer, which concerns all the valid summer LSTs and offsets the temperature anomaly to some extent. It can, therefore, be considered as representative LST for the summer. Furthermore, since the SMLST can well present the characteristic of each summer, it can be compared in the time series. Hence, for the target date, the comparability and representativeness are controlled by the SMLST. In this article, we produced MODIS-like SMLSTs as the target coarse-scale images, with one SMLST for one summer.

D. Reference Pair Selection for the Fine Scale Setup

To conduct the spatiotemporal fusion, the SMLST image is first selected as the target image for the whole summer. The SMLST is required to be fused into a high-resolution image with sufficient spatial details. Thus, effective reference pairs should be selected to provide the spatial details. In other words, the high-resolution image and coarse-resolution image at the reference date should be cloud-free and seamless, so that meaningful spatial details can be retrieved. In the proposed method, the Landsat LSTs are considered as the high-resolution images, and the MODIS-like LSTs are regarded as the coarse-resolution images. Since the MODIS-like images can be retrieved every day, while the Landsat satellite possesses a longer revisit cycle, the major consideration for the reference pair selection lies in the selection of the Landsat images.

If at least one cloud-free Landsat image can be found in a target summer, the corresponding coarse-resolution image is expected to be cloud-free. However, the slight mismatch of the satellite overpass time between the different sensors may lead to the phenomenon of there being some missing pixels in the coarse-resolution images, even though the corresponding Landsat images are cloud-free. In this case, to match with the spatial distribution of the Landsat imagery, a weighted linear regression based multitemporal recovery method (WLR) (software downlink)[5] is used to reconstruct the missing information in the coarse-resolution LSTs [52]. The WLR method requires an auxiliary image to provide the spatial details. In this article, the high-quality coarse-resolution LST close to the date of the reference coarse-resolution LST was selected as the auxiliary image.

As a result of the cloud contamination or other image degradation factors, there may not be any cloud-free Landsat image in a target summer. In this case, the reference pairs from other seasons were taken into consideration. We suggest that the reference pairs are preferred to be selected from early spring to autumn (generally February 15 to November 15 for the northern hemisphere, and August 15 to May 15 for the southern hemisphere, except for whole year for the tropics), to be consistent with the land cover in summer. If there was no cloud-free Landsat image in that stage, the reference pairs from the adjacent years were considered. Since the spatial details for the fusion results are mainly extracted from the reference Landsat image, we should ensure that the spatial detail for the Landsat image is coincident with the ground truth. Thus, we insist to use cloud-free Landsat images at first. If no cloud-free Landsat image could be found for the target year, or for the adjacent years, we recovered the Landsat ETM+ scan line corrector -off images or other Landsat images with less cloud by WLR.

E. Normalization for Comparability

1) Temporal Normalization: The coarse-resolution images used in our study were the MOD11A1 product and the AVHRR product. Actually, limited by the launch time of the Terra satellite, we could not acquire the MOD11A1 product in summer before 2000. Thus, we used the AVHRR product before 2000. The AVHRR LSTs and the MODIS LSTs are not comparable, due to the different sensors and overpass times. Since many researchers have confirmed that the accuracy of the MOD11A1 LST is reliable [53]–[56], if the AVHRR LST could be normalized to be consistent with the MOD11A1 LST (i.e., the MODIS-like LST), we could therefore generate a comparable series of MODIS-like LSTs from 1984 to 2018.

Normalization between AVHRR and MODIS has been widely conducted with the NDVI product [57]–[60]. Referring to these normalization methods for the NDVI products, we propose a normalization method for AVHRR LST and MOD11A1 LST focusing on each pixel in the time series.

Since no MOD11A1 LST could be collected before 2000, the relationship between the AVHRR LST and MOD11A1 LST was established by the data obtained after 2000. We assumed that the relationship is invariable, so that it could be applied to the data before 2000. The AVHRR LSTs and MOD11A1 LSTs for the whole of the summer from 2000 to 2018 were generated and resampled into a 1000-m resolution in UTM projection (1705 pairs, as some MOD11A1 images were missing). Referring

[5][Online]. Available: http://sendimage.whu.edu.cn

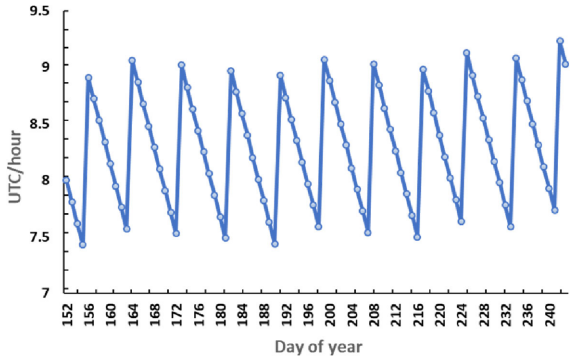


Fig. 4. Overpass times for a pixel at 97.2° E, 29.7° N in summer in 2017.

to the quality assessment field (QA band) obtained from the AVHRR surface reflectance product, the pixels polluted by cloud or cloud shadow were excluded from the AVHRR LST images. As a result of orbit drift, the overpass time for each pixel in the AVHRR LST images varies over a certain period (of around one week; an example is shown in Fig. 4). Considering the diurnal temperature cycle ([18], [39], [61], [62]), for AVHRR LSTs, it would be more reasonable to calculate different normalization coefficients corresponding to the different overpass times. For each pixel location, the overpass times for the 1705 pairs were transferred into integer values. Next, the LSTs for the 1705 pairs were classified into several clusters based on the integer overpass times. To obtain a more robust relationship between the AVHRR LSTs and MODIS LSTs, for each cluster, robust regression according to Huber's M-estimator was conducted [63]. In the traditional framework of the least-squares solver, the function between the AVHRR LSTs and MODIS LSTs can be simply interpreted as

$$\begin{aligned}\mathrm{LST}_{M1000}(x,y,t) = f(x,y,t) \times \mathrm{LST}_{A1000}(x,y,t) \\ + g(x,y,t) + e_2(x,y,t)\end{aligned} \tag{2}$$

where *x, y,* and *t* indicate target pixels (*x, y*) at integer overpass time *t* in the 1705 pairs in summer from 2000 to 2018. LST_{M1000} is the MODIS LST at a 1000-m resolution. LST_{A1000} is the AVHRR LST at a 1000-m resolution. f and g are the linear regression coefficients. e_2 is the residual. For each cluster (target *t*), the sum of squared residuals e_2 should be minimized. However, impacted by the image quality of the AVHRR images, the outliers in the fitting samples have an adverse effect on the regression model. Hence, the weighted least squares estimator is introduced to weaken the influence of the outliers and strengthen the robustness of the model by minimizing the sum of the weighted and squared residuals

$$\min \sum_{x,y} w(x,y)(e_2(x,y))^2 \tag{3}$$

where *w(x, y)* is the corresponding weight, which adjusts the impact of every pixel*(x, y)* in target *t*, and should decrease as the residual e_2 increases. In this study, *w(x, y)* was calculated by Huber's M-estimator

$$w(x,y) = \frac{1}{\max(1, |r(x,y)|)} \tag{4}$$

$$r(x,y) = \frac{e_2(x,y)}{\mathrm{tune} \times (\mathrm{med}(|e_2(x,y) - \mathrm{med}(e_2(x,y))|))/0.6745} \tag{5}$$

where tune is a given parameter (usually 1.345), which can be adjusted. med(∗) is the median function. As a result of the adaptive weights, we can generate new regression coefficients f_m and g_m. Hence, a set of regression coefficients corresponding to the different overpass times for each pixel could be gained.

For each pixel in reference AVHRR images before 2000, its normalization coefficients (f_m and g_m) could be found by searching for the overpass time. The reference AVHRR LST could then be normalized by applying the normalization coefficients corresponding to the different overpass times, assuming that the normalization coefficients are fixed for a target pixel at a target overpass time *t* for different years. After temporal normalization, one mean MODIS-like LST image for one summer could be generated (i.e., the MODIS-like SMLST for each summer as the target image).

2) Spatial Normalization: For the original selected reference pairs in the above step, the error between the Landsat LST and MODIS-like LST is not constant. In brief, most LST inversion methods for Landsat are based on a single thermal band [36], [44], [64], while the MOD11A1 product and AVHRR LST are obtained from multiple-thermal bands [46], [47], [65], [66], inevitably resulting in an error between the Landsat LST and MODIS-like LST. Generally, the inversion error of Landsat is greater than that of MODIS, which leads to a less stable series of Landsat LST compared with MODIS-like LST. In other words, the error between the reference Landsat LST and reference MODIS-like LST does not remain the same as the reference date changes, leading to different fusion results by different reference pairs. Thus, an LST normalization method was developed to correct the error between the Landsat LST and MODIS-like LST to reduce the variation for different reference pairs in the spatial area and assures the comparability between different sensors.

Since the MOD11A1 LST has been verified to be a reliable data [53]–[55], we attempt to set the MODIS-like LST as the reference axis to deduce the system error between MODIS-like LST and Landsat LST. For all reference pairs, the land covers have been classified into two categories, impervious surface and pervious surface. The impervious surface is gained from our previous research [67]. The other land covers are all classified as pervious surface. Next, the average LST and standard deviation for each land cover of each reference pair are calculated. Furthermore, for each land cover in each pair, the difference between the average LST of Landsat and MODIS-like images can be generated

$$\mathrm{DALST}_{LC,j} = \mathrm{LALST}_{LC,j} - \mathrm{MALST}_{LC,j} \tag{6}$$

where *LC* represents for the land cover, i.e., impervious surface or pervious surface. *j* stands for the *j*th reference pair. LALST is the average LST of Landsat image, and MALST is the average LST of MODIS-like image. DALST is the difference between the average LST of Landsat and MODIS-like images.

Similarly, for each land cover in each pair, the difference between the standard deviation of Landsat and MODIS-like

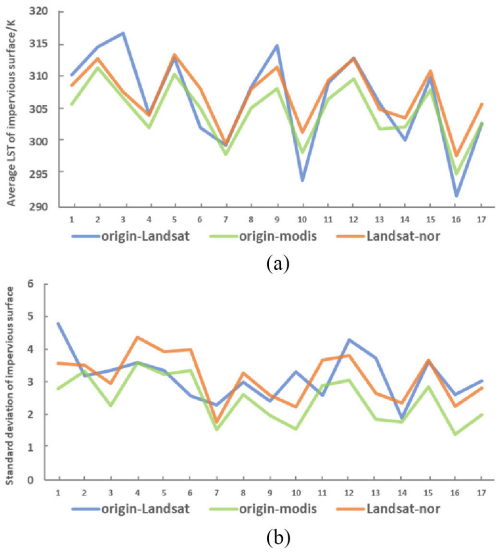


Fig. 5. Expected normalized series of Landsat LST for impervious surface. (a) Average LST. (b) Standard deviation.

images can be generated

$$\mathrm{DSTD}_{LC,j} = \mathrm{LSTD}_{LC,j} - \mathrm{MSTD}_{LC,j} \tag{7}$$

where *LC* and *j* are the same with the above. LSTD is the standard deviation of landsat image, and MSTD is the standard deviation of MODIS-like LST. DSTD is the difference between the standard deviation of landsat and MODIS-like LSTs.

Sequentially, the mean of all the DALST for impervious and pervious surface can be gained (MDALST_i, and MDALST_p, respectively), so does the standard deviation (MDSTD_i, and MDSTD_p, respectively). These means are regarded as the system error between Landsat and MODIS-like images. In other words, for a target land cover of one reference pair, the expected average LST of Landsat image should be the addition of average LST of MODIS-like image and system error, so does the standard deviation

$$\mathrm{EALST}_{LC,j} = \mathrm{MALST}_{LC,j} + \mathrm{MDALST}_{LC} \tag{8}$$

$$\mathrm{ESTD}_{LC,j} = \mathrm{MSTD}_{LC,j} - \mathrm{MDSTD}_{LC} \tag{9}$$

where *LC* and *j* are the same with the above. EALST is the expected average LST of landsat image, and ESTD is the expected standard deviation of landsat image.

Thus, according to the moment matching [68], [69], we can normalize the Landsat images into a more stable series

$$\mathrm{NLST}_{LC,j,x,y} = (\mathrm{LST}_{LC,j,x,y} - B_{LC,j,x})/A_{LC,j,x} \tag{10}$$

where

$$\begin{cases} A_{LC,j,x} = \frac{\mathrm{LSTD}_{LC,j}}{\mathrm{ESTD}_{LC,j}} \\ B_{LC,j,x} = \mathrm{LALST}_{LC,j} - \mathrm{EALST}_{LC,j}\frac{\mathrm{LSTD}_{LC,j}}{\mathrm{ESTD}_{LC,j}} \end{cases} \tag{11}$$

where *LC* and *j* are the same with the above. *x* and *y* are the pixel location. NLST is the normalized Landsat LST we expect to gain. LST is the LST value for each pixel of each category. Taking the impervious surface as example, the temporal trend of the normalized Landsat LST series (see Fig. 5, Landsat-nor) is expected to be more similar with MODIS-like LST series (see Fig. 5, origin-MODIS) compared with the origin Landsat LST series (see Fig. 5, origin-Landsat). The normalized Landsat LST and the corresponding MODIS-like LST are selected as the final reference pair to conduct the spatiotemporal fusion.

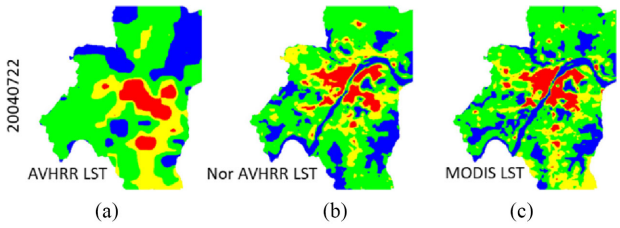


Fig. 6. AVHRR LST, normalized AVHRR LST and the corresponding MOD11A1 LST for July 22, 2004. For each image, the red area is the top 7.5% LST; the yellow area is the top 7.5%–25% LST; the green area is the top 25%–80% LST; the blue area is the last 20% LST.

IV. Results

A. Accuracy Assessment for the Long-Term Coarse-Scale Images

The long-term coarse-scale images generated in this study were a MODIS-like dataset, which included the MOD11A1 LSTs after 2000 and the normalized AVHRR LSTs before 2000. Since the accuracy of the MODIS products has been tested to be reliable in previous research, the accuracy for the whole MODIS-like dataset depends on the temporal normalization between the AVHRR LSTs and MODIS LSTs. The temporal normalization between the AVHRR LSTs and MODIS LSTs is aimed at adjusting the AVHRR LSTs to be consistent with the MODIS LSTs, so that continuous MODIS-like LSTs from 1984 to 2018 can be generated. In this article, we normalized the AVHRR LSTs before 2000 with the regression coefficients generated by the AVHRR LSTs and MOD11A1 products for 2000–2018. Due to the lack of MOD11A1 products before 2000, we could not directly estimate the accuracy of the normalized AVHRR LSTs from 1984 to 1999. Thus, to test the accuracy of the normalization in the time series, a simulated experiment was carried out between the AVHRR LSTs and the MOD11A1 products for 2000–2018.

In detail, we applied the regression coefficients to the AVHRR LSTs for 2000–2018, so that the normalized AVHRR LSTs could be compared with the MOD11A1 product at the same time. An example of the original AVHRR LST on 2004/07/22 can be seen in Fig. 6(a). The corresponding MODIS LST is shown in Fig. 6(c). Based on the normalization method described in Section III-(A), the normalized AVHRR LST can be seen in Fig. 6(b). Comparing the original AVHRR LST and the normalized result, it is clear that more effective information has been added into the AVHRR LST.

For the temporal trends, from Fig. 7, it can be figured out that the AVHRR LST (gray line) has increased a lot after normalization, and the temporal trend for the normalized AVHRR LST (blue line) is smoother than the original AVHRR LST. Furthermore, the values and temporal trends for the normalized AVHRR LST are similar to the MODIS LST (orange line). Overall, the normalized AVHRR LST is tested to be consistent with the MODIS LST, as expected.

TABLE II
SUMMER LSTS GENERATED BY THE DIFFERENT METHODS

Dates	Urban LST (K)			Suburban LST (K)			UHII (K)		
	single	fusion	nor&fusion	single	fusion	nor&fusion	single	fusion	nor&fusion
2002/01/30	282.48	306.14	311.06	281.48	301.21	305.02	1.00	4.93	6.04
2000/02/26	290.20	309.58	311.25	287.16	303.76	306.12	3.04	5.82	5.13
2002/03/19	306.67	315.20	310.85	301.16	308.70	304.89	5.51	6.50	5.96
2003/04/15	299.93	302.96	310.89	295.35	299.33	305.19	4.58	3.63	5.70
2001/05/03	318.24	319.06	310.91	310.33	311.91	305.27	7.91	7.15	5.64
2001/07/22	304.83	305.90	310.22	300.67	302.64	305.06	4.16	3.26	5.16
2001/09/24	310.64	312.41	310.73	307.39	307.09	305.20	3.25	5.32	5.53
2002/10/13	312.70	317.74	310.99	308.70	311.25	305.18	4.00	6.49	5.81
2001/11/27	290.30	309.70	311.22	288.43	304.30	305.56	1.87	5.40	5.66
2001/12/29	279.43	304.72	311.15	278.61	299.82	305.01	0.82	4.90	6.14

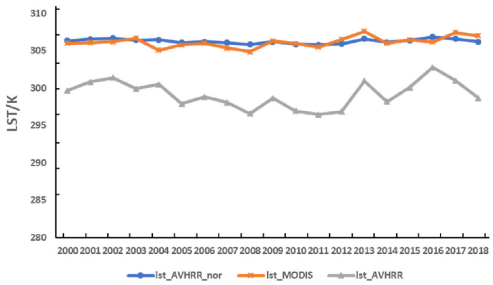


Fig. 7. Temporal trends for the AVHRR LST, normalized AVHRR LST and MODIS LST for Wuhan. lst_AVHRR_nor is the normalized AVHRR LST; lst_MODIS is the MODIS LST; lst_AVHRR is the original AVHRR LST.

B. Accuracy Assessment for the Comparable and Fine-Scale Results

With the assistance of the selected suitable inputs, the comparable and fine-scale LSTs can be generated by the spatiotemporal fusion. Given that the accuracy for the input coarse-scale images has been estimated to be reliable in the above section, if the relationship between the high-resolution and coarse-resolution images can also be confirmed as reliable, then the accuracy of the fusion LSTs can be accepted. In other words, the accuracy of the fusion results is dependent on the spatial normalization between the Landsat LSTs and MODIS-like LSTs. To assess the spatial normalization accuracy, a validation experiment was carried out in Wuhan. The MOD11A1 SMLST covering Wuhan in 2001 was selected as the target image to conduct the spatiotemporal fusion. The landsat images of several days (see Table II) and the corresponding MOD11A1 images were chosen as the reference pairs. The fusion results by different reference pairs were obtained. The average fusion LSTs (landsat-like LSTs) for the urban area (urban LSTs) (with the urban definition referring to [22]) and suburban area (suburban LSTs) (with the suburban definition referring to [21]) were compared with the single-day Landsat LST (single).

The LST accuracies can be inferred from Table II. Focusing on the single-day landsat LST (single), we would obtain different summer LSTs if we chose different days to represent the whole summer (e.g., 318.24K for the urban LST on May 3, 2001, 304.83K for the urban LST on July 22, 2001). If we selected the SMLST as the target image to obtain fusion results, but without normalization (fusion), the fusion LSTs by the reference pairs from other seasons (spring, autumn and winter) would be increased to closer to the summer LST, compared with the single-day LSTs (e.g., 282.48K for the urban LST on January 30, 2002, but 306.14K for the urban LST in fusion result by the reference pair on January 30, 2002). What's more, if the fusion results were generated by normalized reference pairs and target SMLST (nor and fusion), we could generate a relatively uniform SMLST, no matter which reference pair was selected. In detail, focusing on the fusion results by reference pairs with (nor and fusion) and without normalization (fusion), we can find that the difference in the fusion results from different reference pairs is narrowed by the normalization, for urban LST, suburban LST and the UHI intensity (UHII) (e.g., without normalization: 319.06K for the urban LST on reference date May 3, 2001 and 305.90K for the urban LST on reference date July 22, 2001; with normalization: 310.91K for the urban LST on reference date May 3, 2001 and 310.22K for the urban LST on reference date July 22, 2001). We can therefore conclude that the numerical difference between the different reference pairs has been reduced by the spatial normalization.

The accuracy for the spatial details of the fusion results with normalized reference pairs can be figured out from Fig. 8. After normalization, the built-up area (total area of yellow and red for each image in Fig. 8) for the fusion results generated from the reference pairs in different months are almost the same. However, the spatial details for non-built-up areas (mainly vegetation and water bodies, i.e., green and blue areas for each image in Fig. 8) vary with the month. More specifically, the reference pairs from late February to October generate fusion results with similar details in the nonbuilt-up areas (the Yangtze River presents as green in January, November, and December). This is also why we suggest that the reference pairs should be selected from early spring to autumn. In that stage, we can establish that the spatial

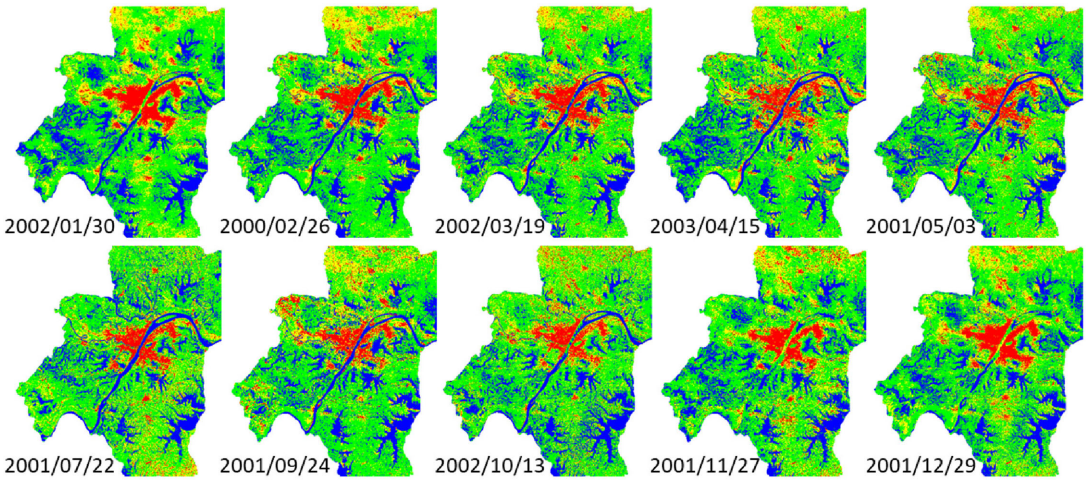


Fig. 8. Spatiotemporal fusion results by different normalized reference pairs in Wuhan. The dates for the reference pairs are listed below the fusion results. For each image, the red area is the top 7.5% LST; the yellow area is the top 7.5%–25% LST; the green area is the top 25%–80% LST; and the blue area is the last 20% LST.

details of the fusion results will remain almost the same for all the normalized reference pairs.

In general, taking the MODIS-like SMLST as the target image, after spatial normalization for reference pairs, the spatial and temporal details of fusion results from different normalized reference pairs are almost the same, for all the reference dates. Thus, the normalization method effectively bridges the gap between the different reference pairs. In other words, if the target image is fixed, after normalizing the reference pairs, we can generate a relatively uniform fused LST no matter which reference pair is selected.

C. Comparable and Fine-Scale Dataset for Wuhan

Wuhan is selected as the validation case to show the results obtained by the procedure designed in this research. One cloud-free reference pair was chosen for one year from 1984 to 2018 in Wuhan. Finally, 30 reference pairs (except 1984, 1985, 1986, 2007, and 2012) were selected to conducted STNLFFM. All the input images for the fusion are given in Table III.

Firstly, the AVHRR LSTs were normalized in the time series to be consistent with the MOD11A1 LSTs by the use of the robust regression coefficients generated from the AVHRR LSTs and MOD11A1 LSTs for 2000–2018. Since there are some missing pixels in the reference MOD11A1 LST images in some years, some high-quality MOD11A1 LSTs were collected as auxiliary data to conduct the WLR method to recover the missing pixels. Thus, a continuous time series of MODIS-like LSTs for the reference dates and MODIS-like SMLSTs for the target dates for Wuhan from 1984 to 2018 was generated. The landsat LSTs at the reference dates were then normalized into a stable series. Lastly, the normalized landsat LSTs and corresponding MODIS-like images at the reference dates, and the MODIS-like SMLSTs at the target dates were utilized to produce the landsat-like SMLSTs for Wuhan.

All the fusion results are shown in Figs. 9 and 10. For the temporal analysis, a continuous LST evolution from 1984 to 2018 can be illustrated (see Fig. 9, blue line). Since the generated fusion LSTs can be deemed as representative and comparable,

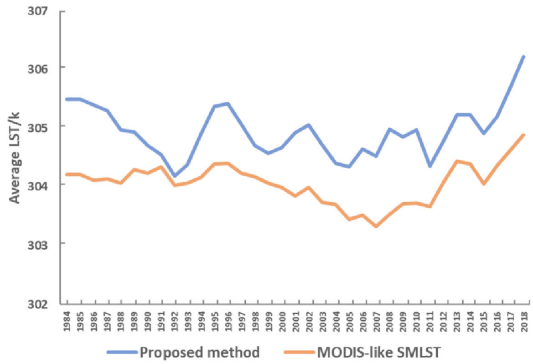


Fig. 9. Average LST of Wuhan from 1984 to 2018. The blue line is the average LST generated in this study; the orange line is the average LST of the MODIS-like SMLSTs, i.e., the average LST of normalized AVHRR SMLSTs before 2000 and MOD11A1 SMLSTs after 2000.

we can point out that the LST evolution trend in Wuhan decreased at first and then increased, with the maximum LST of 306.22K occurring in 2018. From Fig. 9, we can also figure out that the LST generated in this research presents a similar trend with the LST generated by the MODIS-like SMLSTs (orange line), but the numeric range is greater with higher peaks and lower valleys.

For the spatial analysis (see Fig. 10), it can be clearly seen that the fusion results include sufficient spatial information. Thus, a more refined analysis can be carried out. For the spatial analysis, a clear UHI distribution can be determined from the fusion results. It is obvious that the area with higher LST (red and yellow area) for Wuhan was centralized at first and then scattered over the past three decades. A remarkable UHI core is found in Wuhan metropolis and the progress of urbanization can also be recognized.

Overall, the results generated by the procedure proposed in this research combine the more precise temporal trend from the MODIS-like LSTs and the more refined numeric range and spatial information from the Landsat LSTs.

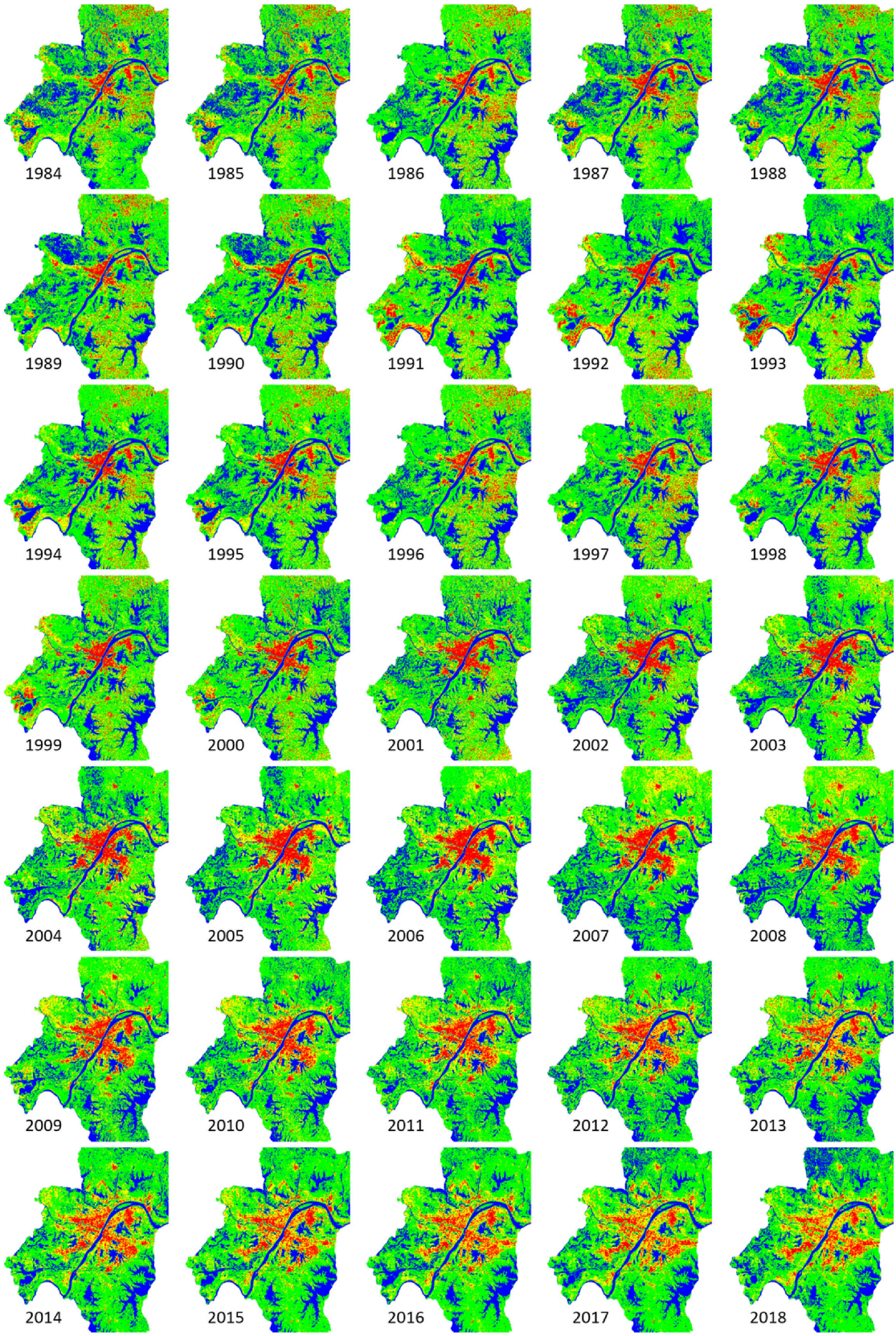


Fig. 10. UHI distribution in Wuhan from 1984 to 2018. For each image, the red area is the top 7.5% LST; the yellow area is the top 7.5%–25% LST; the green area is the top 25%–80% LST; and the blue area is the last 20% LST.

TABLE III
REFERENCE LSTS AND TARGET LSTS FOR THE SPATIOTEMPORAL FUSION IN WUHAN

1984-1999 fusion		2000-2018 WLR		2000-2018 fusion	
Reference pairs	Target images	Auxiliary images	Target images	Reference pairs	Target images
MODIS-like and Normalized Landsat	MODIS-like SMLST	MOD11A1	MOD11A1	MOD11A1and Normalized Landsat	MOD11A1 SMLST
1987/09/26	1984	2000/07/31	2000/09/13	2000/09/13	2000
1987/09/26	1985			2001/07/22	2001
1987/09/26	1986	2002/08/31	2002/09/03	2002/09/03	2002
1987/09/26	1987	2003/06/19	2003/05/01	2003/05/01	2003
1988/08/11	1988			2004/07/22	2004
1989/03/07	1989			2005/04/20	2005
1990/09/02	1990			2006/11/01	2006
1991/07/19	1991			2006/11/01	2007
1992/04/16	1992			2008/04/20	2008
1993/10/12	1993	2009/06/05	2009/09/06	2009/09/06	2009
1994/05/08	1994			2010/11/12	2010
1995/08/31	1995	2011/07/02	2011/06/08	2011/06/08	2011
1996/10/04	1996			2013/06/13	2012
1997/09/21	1997			2013/06/13	2013
1998/10/26	1998	2014/07/21	2014/10/06	2014/10/06	2014
1999/09/27	1999			2015/10/25	2015
		2016/07/26	2016/07/23	2016/07/23	2016
				2017/10/30	2017
				2018/09/15	2018

V. CONCLUSION

In this article, with the help of AVHRR LSTs and MODIS LSTs, we were able to generate a continuous and comparable time series of MODIS-like LSTs by temporal normalization. Furthermore, by integrating the Landsat LSTs and the MODIS-like LSTs by spatial normalization, we could reduce the difference and assure the comparability between the different sensors. What's more, we skillfully took the SMLSTs instead of single-day LSTs for MODIS-like images to represent the whole summer, so that a more accurate representation of each summer could be expressed. Finally, by conducting spatiotemporal fusion between the normalized Landsat LSTs, MODIS-like LSTs, and MODIS-like SMLSTs, a time series of long-term, fine-scale, comparable and representative LSTs for thermal environment monitoring in summer could be gained. Compared with the current studies, our method effectively integrates the high spatial resolution, high temporal resolution, representativeness, and comparability from multisource data.

Overall, we have proposed a framework to produce long-term, fine-scale and comparable SMLSTs, which has the potential for application with other remotely sensed data [e.g., advanced spaceborne thermal emission and reflection radiometer (ASTER) and AVHRR, ASTER and MODIS, etc.], and could serve as a basis for the refined analysis of the thermal environment. Inevitably, there are some limitations to our work. First, if the study area is too cloudy to obtain cloud-free Landsat images in many years (e.g., it is difficult to collect cloud-free Landsat images between 2000 and 2018 for Chengdu, China), the proposed procedure would not take effect, due to the lack of reference pairs. If we could apply other fine-scale remotely sensed data (e.g., ASTER), this problem could be overcome. Second, the spatial resolution of the AVHRR product used in this study is too coarse (0.05°) to provide sufficient spatial information, which increased the difficulty of detecting the land cover changes before 2000. Even though the spatial resolution of MOD11A1 product is much higher than that of AVHRR product, the land cover changes within 1 km^2 are still hard to interpret. The spatiotemporal fusion method inevitably leaves out some changes happening in a certain area, so we insist that the date of reference pairs should be close enough to that of the target image. In our future work, we will focus on the problems and try to provide a more precise dataset for long-term and fine-scale thermal environment monitoring at national or global scale.

ACKNOWLEDGMENT

The authors would like to thank the data providers of the United States Geological Survey Earth Resources Observation and Science Center, the Atmosphere Archive and Distribution System Distributed Active Archive Center, and the National Oceanic and Atmospheric Administration. The authors appreciate the editors and anonymous reviewers for their valuable suggestions.

REFERENCES

[1] T. R. Karl and K. E. Trenberth, "Modern global climate change," *Science*, vol. 302, 2003, Art. no. 1719.

[2] R. Lal, "Soil carbon sequestration impacts on global climate change and food security," *Science*, vol. 304, 2004, Art. no. 1623.

[3] D. Woolf, J. E. Amonette, F. A. Street-Perrott, J. Lehmann, and S. Joseph, "Sustainable biochar to mitigate global climate change," *Nat. Commun.*, vol. 1, pp. 1–9, 2010.

[4] A. Bakun, "Global climate change and intensification of coastal ocean upwelling," *Science*, vol. 247, pp. 198–201, 1990.

[5] L. Hu and N. A. Brunsell, "The impact of temporal aggregation of land surface temperature data for surface urban heat island (SUHI) monitoring," *Remote Sens. Environ.*, vol. 134, pp. 162–174, 2013.

[6] J. M. Norman, M. Divakarla, and N. S. Goel, "Algorithms for extracting information from remote thermal-IR observations of the earth's surface," *Remote Sens. Environ.*, vol. 51, pp. 157–168, 1995.

[7] W. Yu, Z. Nan, Z. Wang, H. Chen, T. Wu, and L. Zhao, "An effective interpolation method for MODIS land surface temperature on the Qinghai–Tibet plateau," *IEEE J. Sel. Top. Appl. Earth Observ. Remote Sens.*, vol. 8, no. 9, pp. 4539–4550, Sep. 2015.

[8] J. A. Voogt and T. R. Oke, "Thermal remote sensing of urban climates," *Remote Sens. Environ.*, vol. 86, pp. 370–384, 2003.

[9] T. R. Oke, "The energetic basis of the urban heat island," *Quart. J. Roy. Meteorol. Soc.*, vol. 108, pp. 1–24, 1982.

[10] M. Roth, T. R. Oke, and W. J. Emery, "Satellite-derived urban heat islands from three coastal cities and the utilization of such data in urban climatology," *Int. J. Remote Sens.*, vol. 10, pp. 1699–1720, 10/01 1989.

[11] D. Streutker, "Satellite-measured growth of the urban heat Island of Houston, Texas," *Remote Sens. Environ.*, vol. 85, pp. 282–289, 2003.

[12] K. Liu, H. Su, X. Li, W. Wang, L. Yang, and H. Liang, "Quantifying spatial–temporal pattern of urban heat island in Beijing: An improved assessment using land surface temperature (LST) time series observations from LANDSAT, MODIS, and Chinese new satellite GaoFen-1," *IEEE J. Sel. Top. Appl. Earth Observ. Remote Sens.*, vol. 9, no. 5, pp. 2028–2042, May 2016.

[13] J. Li, C. Song, L. Cao, F. Zhu, X. Meng, and J. Wu, "Impacts of landscape structure on surface urban heat islands: A case study of Shanghai, China," *Remote Sens. Environ.*, vol. 115, pp. 3249–3263, 2011.

[14] Z. Qiao, G. Tian, L. Zhang, and X. Xu, "Influences of urban expansion on urban heat island in Beijing during 1989–2010," *Adv. Meteorol.*, vol. 2014, pp. 1–11, 2014.

[15] C. Yang *et al.*, "Mapping the influence of land use/land cover changes on the urban heat island effect—A case study of Changchun, China," *Sustainability*, vol. 9, pp. 1–17, 2017.

[16] Q. Weng, M. K. Firozjaei, A. Sedighi, M. Kiavarz, and S. K. Alavipanah, "Statistical analysis of surface urban heat island intensity variations: A case study of Babol city, Iran," *GIScience Remote Sens.*, vol. 56, pp. 576–604, 2019.

[17] Y.-Y. Li, H. Zhang, and W. Kainz, "Monitoring patterns of urban heat islands of the fast-growing Shanghai Metropolis, China: Using time-series of landsat TM/ETM+ data," *Int. J. Appl. Earth Observ. Geoinf.*, vol. 19, pp. 127–138, 2012.

[18] J. Lai *et al.*, "Identification of typical diurnal patterns for clear-sky climatology of surface urban heat islands," *Remote Sens. Environ.*, vol. 217, pp. 203–220, 2018.

[19] S. Cheval and A. Dumitrescu, "The July urban heat island of bucharest as derived from modis images," *Theor. Appl. Climatol.*, vol. 96, pp. 145–153, 2009.

[20] P. Zhang, M. L. Imhoff, R. E. Wolfe, and L. Bounoua, "Characterizing urban heat islands of global settlements using MODIS and nighttime lights products," *Can. J. Remote Sens.*, vol. 36, pp. 185–196, 2010.

[21] M. L. Imhoff, P. Zhang, R. E. Wolfe, and L. Bounoua, "Remote sensing of the urban heat island effect across biomes in the continental USA," *Remote Sens. Environ.*, vol. 114, pp. 504–513, 2010.

[22] S. Peng *et al.*, "Surface urban heat island across 419 global big cities," *Environ Sci Technol*, vol. 46, pp. 696–703, 2012.

[23] X. Gui, L. Wang, R. Yao, D. Yu, and C. Li, "Investigating the urbanization process and its impact on vegetation change and urban heat island in Wuhan, China," *Environ. Sci. Pollut. Res.*, vol. 26, pp. 30808–30825, 2019.

[24] G. C. Miliaresis and A. Tsatsaris, "Mapping the spatial and temporal pattern of day-night temperature difference in Greece from MODIS imagery," *GIScience Remote Sens.*, vol. 48, pp. 210–224, 2011.

[25] H. Shen, L. Huang, L. Zhang, P. Wu, and C. Zeng, "Long-term and fine-scale satellite monitoring of the urban heat island effect by the fusion of multi-temporal and multi-sensor remote sensed data: A 26-year case study of the city of Wuhan in China," *Remote Sens. Environ.*, vol. 172, pp. 109–125, 2016.

[26] B. Chen, B. Huang, and B. Xu, "Comparison of spatiotemporal fusion models: A review," *Remote Sens.*, vol. 7, pp. 1798–1835, 2015.

[27] H. K. Zhang, B. Huang, M. Zhang, K. Cao, and L. Yu, "A generalization of spatial and temporal fusion methods for remotely sensed surface parameters," *Int. J. Remote Sens.*, vol. 36, pp. 4411–4445, 09/02 2015.

[28] H. Shen, X. Li, Q. Cheng, C. Zeng, G. Yang, H. Li *et al.*, "Missing information reconstruction of remote sensing data: A technical review," *IEEE Geosci. Remote Sens. Mag.*, vol. 3, pp. 61–85, Sep. 2015.

[29] E. Arai, Y. E. Shimabukuro, G. Pereira, and N. L. Vijaykumar, "A multi-resolution multi-temporal technique for detecting and mapping deforestation in the Brazilian Amazon rainforest," *Remote Sens.*, vol. 3, pp. 1943–1956, 2011.

[30] W. Zhang *et al.*, "An enhanced spatial and temporal data fusion model for fusing Landsat and MODIS surface reflectance to generate high temporal Landsat-like data," *Remote Sens.*, vol. 5, pp. 5346–5368, 2013.

[31] Q. Cheng, H. Liu, H. Shen, P. Wu, and L. Zhang, "A spatial and temporal nonlocal filter-based data fusion method," *IEEE Trans. Geosci. Remote Sens.*, vol. 55, no. 8, pp. 4476–4488, Aug. 2017.

[32] M. Herrero-Huerta, S. Lagüela, S. M. Alfieri, and M. Menenti, "Generating high-temporal and spatial resolution TIR image data," *Int. J. Appl. Earth Observ. Geoinf.*, vol. 78, pp. 149–162, 2019.

[33] Z. Qian *et al.*, "Association of daily cause-specific mortality with ambient particle air pollution in Wuhan, China," *Environ Res*, vol. 105, pp. 380–389, Nov 2007.

[34] W. Su, C. Gu, and G. Yang, "Assessing the impact of land use/land cover on urban heat island pattern in Nanjing City, China," *J. Urban Plan. Develop.*, vol. 136, pp. 365–372, 2010.

[35] E. Kalnay *et al.*, "The NCEP/NCAR 40-Year reanalysis project," *Bull. Amer. Meteorol. Soc.*, vol. 77, pp. 437–471, 1996.

[36] J. C. Jiménez-Muñoz, "A generalized single-channel method for retrieving land surface temperature from remote sensing data," *J. Geophys. Res.*, vol. 108, pp. 1–9, 2003.

[37] J. C. Jiménez-Muñoz, J. A. Sobrino, D. Skoković, C. Mattar, and J. Cristóbal, "Land surface temperature retrieval methods from Landsat-8 thermal infrared sensor data," *IEEE Geosci. Remote Sens. Lett.*, vol. 11, no. 10, pp. 1840–1843, Oct. 2014.

[38] J. C. Jiménez-Muñoz *et al.*, "Revision of the single-channel algorithm for land surface temperature retrieval from Landsat thermal-infrared data," *IEEE Trans. Geosci. Remote Sens.*, vol. 47, no. 1, pp. 339–349, Jan. 2009.

[39] J. Quan, W. Zhan, T. Ma, Y. Du, Z. Guo, and B. Qin, "An integrated model for generating hourly Landsat-like land surface temperatures over heterogeneous landscapes," *Remote Sens. Environ.*, vol. 206, pp. 403–423, 2018.

[40] P. Fu and Q. Weng, "A time series analysis of urbanization induced land use and land cover change and its impact on land surface temperature with Landsat imagery," *Remote Sens. Environ.*, vol. 175, pp. 205–214, 2016.

[41] P. Fu and Q. Weng, "Consistent land surface temperature data generation from irregularly spaced Landsat imagery," *Remote Sens. Environ.*, vol. 184, pp. 175–187, Jan. 2016.

[42] Z. Wan, "New refinements and validation of the MODIS land-surface temperature/emissivity products," *Remote Sens. Environ.*, vol. 112, pp. 59–74, 2008.

[43] W. Wang, S. Liang, and T. Meyers, "Validating MODIS land surface temperature products using long-term nighttime ground measurements," *Remote Sens. Environ.*, vol. 112, pp. 623–635, 2008.

[44] J. A. Sobrino, J. C. Jiménez-Muñoz, and L. Paolini, "Land surface temperature retrieval from LANDSAT TM 5," *Remote Sens. Environ.*, vol. 90, pp. 434–440, 2004.

[45] J. A. Sobrino *et al.*, "Land surface emissivity retrieval from different VNIR and TIR sensors," *IEEE Trans. Geosci. Remote Sens.*, vol. 46, no. 2, pp. 316–327, Feb. 2008.

[46] D. R. Streutker, "A remote sensing study of the urban heat Island of Houston, Texas," *Int. J. Remote Sens.*, vol. 23, pp. 2595–2608, 2002.

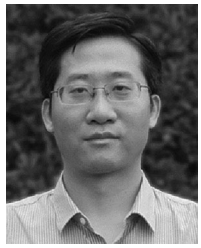
[47] J. C. Price, "Land surface temperature measurements from the split window channels of the NOAA 7 advanced very high resolution radiometer," *J. Geophys. Res.*, vol. 89, pp. 7231–7237, 1984.

[48] J. A. Sobrino and N. Raissouni, "Toward remote sensing methods for land cover dynamic monitoring: Application to Morocco," *Int. J. Remote Sens.*, vol. 21, pp. 353–366, 2000.

[49] J. A. Sobrino, N. Raissouni, and Z.-L. Li, "A comparative study of land surface emissivity retrieval from NOAA data," *Remote Sens. Environ.*, vol. 75, pp. 256–266, 2001.
[50] Y. Julien, J. A. Sobrino, and W. Verhoef, "Changes in land surface temperatures and NDVI values over europe between 1982 and 1999," *Remote Sens. Environ.*, vol. 103, pp. 43–55, 2006.
[51] H. Shen, J. Wu, Q. Cheng, M. Aihemaiti, C. Zhang, and Z. Li, "A spatiotemporal fusion based cloud removal method for remote sensing images with land cover changes," *IEEE J. Sel. Top. Appl. Earth Observ. Remote Sens.*, vol. 12, no. 3, pp. 862–874, Mar. 2019.
[52] C. Zeng, H. Shen, and L. Zhang, "Recovering missing pixels for Landsat ETM+ SLC-off imagery using multi-temporal regression analysis and a regularization method," *Remote Sens. Environ.*, vol. 131, pp. 182–194, 2013.
[53] P. Wu, H. Shen, T. Ai, and Y. Liu, "Land-surface temperature retrieval at high spatial and temporal resolutions based on multi-sensor fusion," *Int. J. Dig. Earth*, vol. 6, pp. 113–133, 2013.
[54] Z. Wan, Y. Zhang, Q. Zhang, and Z. Li, "Validation of the land-surface temperature products retrieved from terra moderate resolution imaging spectroradiometer data," *Remote Sens. Environ.*, vol. 83, pp. 163–180, Jan. 2002.
[55] Z. Wan, Y. Zhang, Q. Zhang, and Z. L. Li, "Quality assessment and validation of the MODIS global land surface temperature," *Int. J. Remote Sens.*, vol. 25, pp. 261–274, 2010.
[56] S. Duan and Z. Li, "Intercomparison of operational land surface temperature products derived from MSG-SEVIRI and Terra/Aqua-MODIS data," *IEEE J. Sel. Top. Appl. Earth Observ. Remote Sens.*, vol. 8, no. 8, pp. 4163–4170, Aug. 2015.
[57] X. Guan, H. Shen, X. Li, W. Gan, and L. Zhang, "Climate control on net primary productivity in the complicated mountainous area: A case study of Yunnan, China," *IEEE J. Sel. Top. Appl. Earth Observ. Remote Sens.*, vol. 11, no. 12, pp. 4637–4648, Dec. 2018.
[58] X. Guan *et al.*, "A 33-Year NPP monitoring study in southwest China by the fusion of multi-source remote sensing and station data," *Remote Sens.*, vol. 9, 2017, Art. no. 1082.
[59] D. Mao, Z. Wang, L. Luo, and C. Ren, "Integrating AVHRR and MODIS data to monitor NDVI changes and their relationships with climatic parameters in Northeast China," *Int. J. Appl. Earth Observ. Geoinf.*, vol. 18, pp. 528–536, 2012.
[60] Y. Liu, R. Liu, and J. M. Chen, "Retrospective retrieval of long-term consistent global leaf area index (1981–2011) from combined AVHRR and MODIS data," *J. Geophys. Res., Biogeosci.*, vol. 117, pp. 1–14, 2012.
[61] F. Hong *et al.*, "Comprehensive assessment of four-parameter diurnal land surface temperature cycle models under clear-sky," *ISPRS J. Photogrammetry Remote Sens.*, vol. 142, pp. 190–204, 2018.
[62] F.-M. Göttsche and F.-S. Olesen, "Modelling the effect of optical thickness on diurnal cycles of land surface temperature," *Remote Sens. Environ.*, vol. 113, pp. 2306–2316, 2009.
[63] X. Li, H. Shen, L. Zhang, H. Zhang, and Q. Yuan, "Dead pixel completion of aqua MODIS band 6 using a robust M-estimator multiregression," *IEEE Geosci. Remote Sens. Lett.*, vol. 11, no. 4, pp. 768–772, Nov. 2014.
[64] Z. Qin, A. Karnieli, and P. Berliner, "A mono-window algorithm for retrieving land surface temperature from Landsat TM data and its application to the Israel-Egypt border region," *Int. J. Remote Sens.*, vol. 22, pp. 3719–3746, 2001.
[65] Z. Wan and Z.-L. Li, "A physics-based algorithm for retrieving land-surface emissivity and temperature from EOS/MODIS data," *IEEE Trans. Geosci. Remote Sens.*, vol. 35, no. 4, pp. 980–996, Jul. 1997.
[66] Z. Wan and J. Dozier, "A generalized split-window algorithm for retrieving land-surface temperature from space," *IEEE Trans. Geosci. Remote Sens.*, vol. 34, no. 4, pp. 892–905, Jul. 1996.
[67] Y. Shen, H. Shen, Q. Cheng, L. Huang, and L. Zhang, "Monitoring three-decade expansion of China's major cities based on satellite remote sensing images," *Remote Sens.*, vol. 12, pp. 1–19, 2020.
[68] H. Shen, W. Jiang, H. Zhang, and L. Zhang, "A piece-wise approach to removing the nonlinear and irregular stripes in MODIS data," *Int. J. Remote Sens.*, vol. 35, pp. 44–53, 2013.
[69] F. Gadallah, F. Csillag, and E. Smith, "Destriping multisensor imagery with moment matching," *Int. J. Remote Sens.*, vol. 21, pp. 2505–2511, 2000.

Yao Shen received the B.S. degree in geographic information system, in 2015 from Wuhan University, Wuhan, China, where she is currently working toward the Ph.D. degree in cartography and geographic Information engineering at the School of Resource and Environmental Sciences.

Her research interests include urban remote sensing in urban expansion and urban thermal environment.



Huanfeng Shen (Senior Member, IEEE) received the B.S. degree in surveying and mapping engineering and the Ph.D. degree in photogrammetry and remote sensing from Wuhan University, Wuhan, China, in 2002 and 2007, respectively.

In 2007, he joined the School of Resource and Environmental Sciences (SRES), Wuhan University, where he is currently a Luojia Distinguished Professor and an Associate Dean of SRES. He was or is the PI of two projects supported by National Key Research and Development Program of China, and six projects supported by National Natural Science Foundation of China. He has authored or coauthored more than 100 research papers in peer-reviewed international journals. His research interests include remote sensing image processing, multi-source data fusion, and intelligent environmental sensing.

Dr. Shen is a Council Member of China Association of Remote Sensing Application, Education Committee Member of Chinese Society for Geodesy Photogrammetry and Cartography, and Theory Committee Member of Chinese Society for Geospatial Information Society. He is currently a member of the Editorial Board of *Journal of Applied Remote Sensing and Geography and Geo-Information Science*.



Qing Cheng received the B.S. degree in the geographic information system and the Ph.D. degree in photogrammetry and remote sensing from Wuhan University, Wuhan, China, in 2010 and 2015, respectively.

She is currently a Lecturer with the School of Urban Design, Wuhan University. Her research interests include remote sensing data reconstruction, data fusion, and urban remote sensing.



Liangpei Zhang (Fellow, IEEE) received the B.S. degree in physics from Hunan Normal University, Changsha, China, in 1982, the M.S. degree in optics from the Xi'an Institute of Optics and Precision Mechanics, Chinese Academy of Sciences, Xi'an, China, in 1988, and the Ph.D. degree in photogrammetry and remote sensing from Wuhan University, Wuhan, China, in 1998.

He is currently a Chair Professor with the State Key Laboratory of Information Engineering in Surveying, Mapping, and Remote Sensing, Wuhan University. He was a Principal Scientist for the China state key basic research project (2011–2016) appointed by the ministry of national science and technology of China to lead the remote sensing program in China. He has authored or coauthored more than 700 research papers and five books. He is the Institute for Scientific Information (ISI) highly cited author. He is the holder of 30 patents. His research interests include hyperspectral remote sensing, high-resolution remote sensing, image processing, and artificial intelligence.

Dr. Zhang is a Fellow of Institute of Electrical and Electronic Engineers (IEEE) and the Institution of Engineering and Technology. He was a recipient of the 2010 Best Paper Boeing Award, the 2013 Best Paper ERDAS Award from the American Society of Photogrammetry and Remote Sensing and 2016 Best Paper Theoretical Innovation Award from the International Society for Optics and Photonics. His research teams won the top three prizes of the IEEE GRSS 2014 Data Fusion Contest, and his students have been selected as the winners or finalists of the IEEE International Geoscience and Remote Sensing Symposium Student Paper Contest in recent years. He also serves as an Associate Editor or Editor of more than ten international journals. He is currently an Associate Editor for the IEEE TRANSACTIONS ON GEOSCIENCE AND REMOTE SENSING. He is the Founding Chair of IEEE Geoscience and Remote Sensing Society Wuhan Chapter.